Gravity wave momentum fluxes estimated from Project Loon balloon data

Brian Green[1], Aditi Sheshadri[1], M. Joan Alexander[2], Martina Bramberger[2], François Lott[3]

[1]Stanford University
[2]NorthWest Research Associates
[3]Laboratoire de Météorologie Dynamique (LMD)/IPSL

Corresponding author: Brian Green (briangre@stanford.edu)

Key Points

- We estimate and analyze atmospheric gravity wave momentum fluxes from Project Loon balloon data collected in the lower stratosphere.
- We use the statistics of the approximately log-normal momentum flux probability distributions to explain inter-regional flux variability.
- Our results can be used as observational constraints when developing and validating gravity wave parameterizations.

Abstract

We present estimates of gravity wave momentum fluxes calculated from Project Loon superpressure balloon data collected between 2013 and 2021. In total, we analyzed more than 5000 days of data from balloon flights in the lower stratosphere, flights often over regions or during times of the year without any previous in-situ observations of gravity waves. Maps of mean momentum fluxes show significant regional variability; we analyze that variability using the statistics of the momentum flux probability distributions for six regions: the Southern Ocean, the Indian Ocean, and the tropical and extratropical Pacific and Atlantic Oceans. The probability distributions are all approximately log-normal, and using only their geometric means and geometric standard deviations we explain the sign and magnitude of regional mean and 99th percentile zonal momentum fluxes, and regional momentum flux intermittencies. We study the dependence of the zonal momentum flux on the background zonal wind and argue that the increase of the momentum flux with the wind speed over the Southern Ocean is likely due to a varying combination of both wave sources and filtering. Finally, we show that as the magnitude of the momentum flux increases, the fractional contributions by high-frequency waves increases, waves which need to be parameterized in large-scale models of the atmosphere. In particular, the near-universality of the log-normal momentum flux probability distribution, and the relation of its statistical moments to the mean momentum flux and intermittency, offer useful checks when evaluating parameterized or resolved gravity waves in models.

Plain Language Summary

Atmospheric gravity waves flux momentum away from their sources, depositing it as drag when they dissipate. Global climate models cannot resolve the entire gravity wave spectrum, so they must parameterize this drag by making assumptions about the gravity wave field developed from wave theory and validated by observations. We present new estimates of gravity wave momentum fluxes observed by Project Loon balloons, which flew on surfaces of constant density in the lower stratosphere and could detect gravity waves using their GPS sensors. The balloons detected significant regional and temporal variability in the momentum fluxes, and we explain this variability using the statistics of the momentum flux probability distributions. We also find that the momentum flux varied with the background wind over the Southern Ocean in ways that point to the competing effects of changing wave sources and filtering of the waves by the background flow, and that high-frequency waves were important contributors to large values of the momentum flux. These new estimates of the momentum flux come from many regions of the stratosphere that have never been sampled by neutral-density balloons before and provide observational constraints for the development and validation of the representation of gravity waves in models.

1 Introduction

Drag induced by dissipating atmospheric gravity waves is one of the most important ways the waves interact with their environment. Because global models of the atmosphere cannot resolve the entire gravity wave (GW) spectrum, they are forced to parameterize this drag by assuming

some range of wave sources, how the waves propagate, and how they dissipate (Plougonven et al., 2020). These assumptions are based on gravity wave theory, results from high-resolution model runs, and comparisons of model output to observations of the waves from both in-situ and remote platforms (see Alexander et al., 2010 for a review).

Among the available in-situ observations, superpressure balloons are uniquely well-suited for measuring gravity waves. Floating approximately on isopycnals, the balloons act as quasi-Lagrangian tracers, and their data time series are analyzed in the intrinsic (flow-following) frequency space that defines the range of vertically propagating GWs. Techniques using wavelet transforms and other similar spectral methods have been developed to estimate the GW momentum flux from balloon data (Boccara et al., 2008; Vincent and Hertzog et al., 2014; Vincent and Alexander, 2020). (The momentum flux is converted to drag when the waves dissipate, but the balloons cannot directly measure the GW-induced drag.) These techniques have been applied to data from past scientific balloon campaigns to estimate the mean GW momentum flux and its statistical distribution (e.g., Hertzog et al., 2008; Jewtoukoff et al., 2015), and the dependence of the momentum flux on the waves' environment, such as their proximity to convection (Corcos et al., 2021).

A drawback to these past scientific balloon campaigns has been their limited number of observations, often from just one region and season. Over a ten-year span, Project Loon launched more than 2000 balloons that flew around much of the globe, sampling many regions of the lower stratosphere for the first time. Loon data have already been used to study gravity waves (e.g., the power spectra of the wind and temperature data: Schoeberl et al., 2017; the near-inertial peak in the wind power spectra: Conway et al., 2019; and the seasonal and latitudinal variability of the slope of wind power spectra: Lindgren et al., 2020), but not yet to estimate GW momentum fluxes.

In this paper, we present gravity wave momentum fluxes estimated from the Loon data. In the next section, we describe the Loon dataset, how we processed the data, and how we estimate the GW momentum flux time series. In section 3 we present maps of the mean total, zonal, and meridional momentum fluxes. In section 4 we decompose the mean zonal flux in six geographic regions into contributions by its eastward and westward momentum flux components, focusing on the properties of their approximately log-normal probability distributions. In section 5 we study the dependence of the zonal momentum flux on the background zonal wind, and in section 6 we study the relationship between the momentum flux and the fractional contributions to its magnitude by high-, medium-, and low-frequency waves. We conclude with a summary and discussion of our results.

2 Processing the Loon balloon data and estimating the gravity wave momentum flux

Our analysis primarily uses GPS data collected by the balloons Loon LLC flew to support their mission of improving global internet coverage (Rhodes & Candido, 2021). From 2011 to 2021, Loon launched 2127 balloons to cruising altitudes between 16 and 21 km. In aggregate, the balloons flew above most of the globe, but some large regions such as Europe and Asia have almost no data coverage. The balloons measured their position (with GPS; uncertainty +/-2.5 m), and ambient pressure (uncertainty +/- 1 hPa) and temperature (uncertainty +/- 5 K) every 60 seconds. From the GPS data, Loon provides derived zonal and meridional winds. The uncertainties in the pressure and temperature data are too large to reliably detect gravity waves,

so we exclusively used the GPS data, which have uncertainties similar to past scientific balloon campaigns (e.g., Podglajen et al., 2016).

An important difference to those campaigns is the maneuvering the Loon balloons performed to alter their horizontal trajectories. Times when the balloons were maneuvering vertically by changing their density, or horizontally by using a propellor, are indicated in the data by flags. When maneuvering occurred, we split a flight's data into "segments" of time when the balloon is passively drifting, then analyzed those segments separately. To make sure the data sampled a large part of the GW frequency spectrum, we only analyzed the 938 segments that were at least two days long. These yielded 5245 days of observations, several times more data than the Strateole/Vorcore (Hertzog et al., 2007) and Concordiasi (Rabier et al., 2010) campaigns, which were each limited to one geographic region and season.

The GPS data contain measurement errors that we wanted to eliminate and not falsely interpret as gravity waves. Errors in the GPS data commonly appear as spikes in the wind or altitude data. If the zonal or meridional wind changed by more than 2 m/s over a 60-second interval from one data point to the next, and the following change was also more than 2 m/s (again, over 60 seconds) but opposite in sign, we removed the spike in the data by setting its value to the prior data point (as in Lindgren et al., 2020). Spikes in the altitude data larger than 100 m were treated identically. In both the wind and altitude data, there are also several obvious spikes that last longer than one time step. Using the same amplitude criteria as before, we identified these manually and interpolated across the bad data, deleting 20 spikes in the wind data and 32 spikes in the altitude data.

Occasionally, the balloons experienced altitude changes of more than 100 m that are clearly not associated with gravity wave motion. These changes often happened at either the beginning or end of the segment, indicative of the termination or initiation of maneuvering, but were sometimes associated with depressurization events, which can happen at night when the balloon's cooled enough to lose superpressure relative to its environment (Corcos et al., 2021). We manually identified 78 non-GW altitude changes, and those data were removed from our analysis.

Though the balloons collected data every 60 seconds, transmission errors occasionally resulted in gaps of several minutes, so after we checked the data for maneuvering, spikes, and non-GW altitude changes, we interpolated it onto an evenly spaced two-minute time step using cubic interpolation.

Vertical velocity anomalies due to adiabatic gravity waves in a compressible atmosphere are associated with the displacement of isentropes, not the isopycnals the balloons flew on, but the two are related by the temperature lapse rate in the waves' environment (see Equations 6 and 7 in Vincent & Alexander, 2020). We used COSMIC-1 (Anthes et al., 2008) and COSMIC-2 (Yue et al., 2014) radio occultation data to estimate the environmental temperature and its lapse rate. At each time step, we averaged together COSMIC temperature profiles measured within 1 day, 2.5° latitude, and 60° longitude of the balloon to define the environmental profile, then took its vertical derivative and interpolated both profiles to the balloon's altitude. From the interpolated lapse rate, we then calculated the factor (typically 3-4) used to scale up displacements of the isopycnic surface and applied its segment-mean value to the detrended balloon altitude anomalies. Finally, we took the centered difference of the scaled-up altitude anomalies to estimate the isentrope's anomalous vertical velocities.

Following the methodology laid out in Torrence and Compo (1998), we used continuous wavelet transforms to estimate the gravity wave momentum flux. Wavelets resolve signals in

time and frequency and are popular for analyzing balloon data (e.g., Corcos et al., 2021; Hertzog et al., 2008; Jewtoukoff et al., 2015) because gravity waves are intermittent and propagate in a limited range of frequencies. We balanced resolution in the time and frequency dimensions by using a Morlet wavelet with a nondimensional frequency ω_0 of 4 (we also performed the analysis with an ω_0 of 6, which sacrifices time for frequency resolution, and the results didn't change enough to affect our conclusions). We performed wavelet analyses on each segment's time series of zonal (u), meridional (v), and vertical (w) wind anomalies, setting the complex amplitude coefficients with magnitudes smaller than three times the instrumental uncertainty to zero. To reduce the effects of the wavelet's cone of influence, after performing the analysis we deleted the first and last two hours of data from each segment.

Our method for calculating time series of the upward flux of zonal momentum from the wavelet coefficients is shown in Figure 1. (To calculate the upward flux of meridional momentum, replace u with v wavelet coefficients.) First, we calculate the cross-wavelet spectrum of u and w and retain only the real-valued coefficients. Then we take weighted sums (see Eq. 24 of Torrence & Compo, 1998) over the GW period range of the positive and negative coefficients, separately, to get two time series, one each of the upward flux of eastward and westward momentum. From now on we will refer to these as the eastward and westward momentum fluxes. (To our knowledge, this method of separating the positive and negative coefficients has been applied once before, in section 5.3 of Corcos et al., 2021.) We used a minimum period of 10 minutes to avoid the shorter periods when the balloons depart significantly from their isopycnals (see Fig. 3 of Vincent & Hertzog, 2014), and a maximum period of either one day or the Coriolis period, whichever was smaller. To convert the flux time series to units of Pascals, we multiply them by the segment-mean density, estimated from the balloon's pressure measurement and the COSMIC temperature data. For the data segment shown in Figure 1, the eastward and westward fluxes are a few millipascals when the balloon was above the Southern Ocean before jumping to over 200 mPa westward when it flew over the Andes at the tip of South America.

We have also calculated, but will not present, the gravity wave pseudo-momentum flux, which differs from the momentum flux by the factor $(1 - f^2/\omega^2)$ and is related to the gravity wave contribution to the Eliassen-Palm flux (Eq.'s 41 and 42, Fritts and Alexander, 2003; f is the Coriolis frequency and ω is the frequency in the reference frame of the balloon). The differences between these two versions of the momentum flux are negligible in our results in sections 2-5 and minor in for those in section 6, where we discuss them further.

It is more common to combine superpressure balloons' pressure data with the equations presented in Boccara et al. (2008) and Vincent and Hertzog (2014) to estimate the momentum flux than to use vertical velocities derived from the GPS altitude (e.g., Vincent & Alexander 2020). In past scientific campaigns, balloons' pressure sensors have been more sensitive to vertical motion than GPS, but the large uncertainties in the Loon pressure data make the altitude data more accurate. One advantage of using altitude data to estimate momentum fluxes, instead of using pressure data, is not having to assume that the GWs measured by the balloons behave according to their linear polarization relations. As mentioned above, we discarded the w amplitude coefficients if they were less than three times the amplitude associated with uncertainties in the altitude data. Figure 1 shows that, when the momentum flux is larger than a few millipascals, the Loon GPS sensor was sufficiently sensitive to detect GWs at even their highest frequencies.

3 Maps of mean momentum fluxes

Figure 2 shows maps of mean momentum fluxes, calculated by binning the momentum flux time series into 5° latitude by 10° longitude grid cells and averaging, making the mean fluxes averages over time and space. The mean total (non-directional) momentum flux is in general largest over the Southern Ocean, where it regularly exceeds 15 mPa. Over much of the rest of the global ocean, it is typically less than 5 mPa, except over the northern hemisphere Atlantic where it's noticeably larger, 5-10 mPa. This range of values is also commonly observed over the Americas and Africa, except in some cases when the balloons passed over mountain ranges. In the tropics, the magnitude of the mean total momentum flux – several mPa with maxima near 10 mPa – is close to estimates from the Strateole-2 superpressure balloons (see Figure 11 of Corcos et al., 2021).

Particularly for the zonal momentum fluxes, there are large-scale patterns of the sign of the flux, generally westward in the mid-latitudes and often eastward in the tropics. (Between 30 and 60 °S, the area-weighted mean zonal flux is -2.52 mPa; between 30 and 60 °N, it is -0.62 mPa; between 15 °S and 15 °N, it is -0.20 mPa, but there are large regions over the Indian and Pacific Oceans where it is positive.) Large-scale patterns in the meridional momentum fluxes are less obvious, but there is a slight difference between the hemispheres: its area-weighted mean in the Southern Hemisphere is slightly positive and pointed toward the equator (0.25 mPa), while it is nearly zero in the Northern Hemisphere (0.01 mPa).

The momentum flux maps have several interesting local features. Over parts of northern Africa there are relatively high fluxes, possibly due to orographic gravity waves generated in the vicinity of the Hoggar and Atlas Mountains; 13 balloons flew over or near those mountain ranges. For those flights, the magnitude of the momentum flux regularly exceeds 20 mPa above the mountains, with maxima above 100 mPa. The largest amplitude momentum fluxes in the Loon dataset, though, are found over the Andes. Of the 89 flights that passed over the tip of South America, 57 of them show westward momentum fluxes there larger than 50 mPa, with the largest westward flux almost 2 Pa. Also, the mean zonal and total momentum flux magnitudes above the Andes are larger than indicated in Figure 2, where the color scales saturate at 10 and 20 mPa, respectively. In the grid cells from 35 to 55 °S and 60 to 80 °W, the mean zonal momentum flux is -13.97 mPa and the minimum is -41.90 mPa. In those same grid boxes, the mean total momentum flux is 36.97 mPa, and the maximum is 104.88 mPa. For comparison, the mean total momentum flux above the Antarctic peninsula, measured at 19 km altitude during the Concordiasi balloon campaign, is about 100 mPa (see Fig. 1d of Jewtoukoff et al., 2015).

Though comparisons between different observing platforms are difficult, it seems our estimated mean momentum fluxes of more than 100 mPa over mountains aren't inconsistent with those calculated from data from research aircraft flights in the middle and upper troposphere. Lilly and Kennedy (1973) estimated an average momentum flux over a 200 km path of about 1 Pa at altitudes of 6-8 km in a region of severe turbulence above the Rockies. The PYREX field program found peak momentum fluxes of several Pa above the Pyrenees and averages along 300 km flight legs of about 500 mPa at 12 km altitude (Lott, 1995). More recently, the DEEPWAVE campaign measured flight-leg-average fluxes at 12 km altitude above New Zealand of several hundred mPa; the average leg length was 350 km (Smith et al., 2016). From 06:00 to 18:00 UTC on March 14, 2014, the Loon balloon shown in Figure 1 traveled 355 km at an average altitude of 20.5 km; during this period, we estimate a mean total momentum flux of 59 mPa. Though this

value and the mean total momentum fluxes of about 100 mPa discussed above are significantly lower than those estimated from the aircraft data, the Loon balloons flew at much higher altitudes than the aircraft, and orographic gravity wave momentum fluxes are believed to reduce significantly with height in the upper troposphere due to the interaction of the waves with, for example, clear air turbulence.

Loon coverage was uneven in space and time, and the momentum flux maps should not everywhere be interpreted as a climatology. Figure 3 gives a sense of the seasonal and interannual variability of the balloons' regional coverage, showing time series of the monthly fraction of the total data collected in each of the colored regions demarcated in the top panel. In the Tropical Atlantic and Tropical Pacific Oceans, the amount of data collected varies significantly from month to month, but over the length of the record each season was well-sampled. (n.b. We name regions according to the ocean basins the balloons flew over, referring to the data as collected "in" a region, and do not mean to imply that the data were collected inside (below the surface of) the ocean.) For the other regions, the Extratropical Pacific, the Extratropical Atlantic, the Indian Ocean, and the Southern Ocean, there were significant biases in the seasonal coverage. In the Extratropical Atlantic, for example, winter was better sampled than summer: 65% of the data there were collected between November and February. In the Southern and Indian Oceans, the majority of the data were collected during several months of one year, in the second half of 2014 in the Southern Ocean, and in late 2020 to early 2021 in the Indian Ocean. These sampling biases do not diminish the utility of Figure 2, since many regions and seasons have lacked balloon observations until Project Loon, but we mention them to clarify that the maps do not display the true annual mean gravity wave momentum fluxes in the balloon altitude range. In some cases, such as the Southern Ocean where most of the data were collected in the winter months when the westerly jet is strongest, the seasons with the most data are those of the most interest.

4 Regional momentum flux probability distributions

To better understand the range of gravity waves contributing to the mean zonal momentum flux, in this section we analyze the eastward and westward components of the flux and their probability distributions for the six regions shown in Figure 3. There is very little land in any of the regions, so the gravity waves measured in them most likely had non-orographic sources. We're focusing on non-orographic gravity waves because they represent a major source of uncertainty in climate models' gravity wave parameterizations (Alexander et al., 2010; Plougonven et al., 2020), and on their zonal momentum fluxes because that component has the most regional variability and drives important patterns of wind variability, such as the Quasi-Biennial Oscillation and the polar vortices (reviewed in Alexander et al., 2010). Selecting three mid-latitude and three tropical regions ensures our analysis samples waves from a variety of non-orographic sources, though we do not distinguish between those sources beyond our choice of region boundaries. In the Tropical Pacific, for example, our focus is on waves in the vicinity of the convection in the Inter-Tropical Convergence Zone, so that region is centered in latitude on the climatological position of the ITCZ. Each region's boundaries are fixed in time.

Before discussing the probability distributions, we present in Table 1 each region's mean zonal momentum flux and its decomposition into its mean eastward and westward components. By construction, the number of samples of the eastward and westward momentum fluxes are

equal (Figure 1), so the mean zonal momentum flux is equal to the difference between the mean eastward and mean westward momentum fluxes. For all six regions, the magnitude of the zonal flux is smaller than both the eastward and westward fluxes. In the Indian and Pacific Oceans, it's more three times smaller than either component. This is true for the decomposition of the mean meridional momentum flux into its northward and southward components, too (not shown). These averages are taken over many thousands of data points spread over large geographic regions, and it should be noted that, as Figure 1 shows, the instantaneous momentum flux or its local mean can be almost unidirectional. But, over a large enough region and a long enough time, we find that the mean zonal and meridional momentum fluxes by non-orographic gravity waves are the residual of larger opposite-signed fluxes.

Figure 4 shows the probability density distributions of the eastward and westward momentum fluxes for each region. The distributions are approximately log-normal – that is, the probability density of the logarithm of the independent variable (the momentum flux) is approximately normally distributed – a characteristic that's been noted in both numerical simulations of non-orographic gravity waves and in balloon and satellite observations (e.g., Hertzog et al., 2012; Plougonven et al., 2017; Lott et al., 2023). Like the normal distribution, the log-normal distribution is described by two statistical moments, the geometric mean and geometric standard deviation. Table 2 gives the geometric means and geometric standard deviations of the eastward and westward momentum flux probability distributions for each region.

Throughout this paper, we will refer to both the geometric mean of a momentum flux probability distribution and the mean momentum flux; the two are related but distinct. Both are averages of the same data: the geometric mean is the mean of the logarithm of the flux values and is dimensionless, and the mean momentum flux is the mean of the dimensional fluxes and has units of mPa. (Similar to the geometric mean, the geometric standard deviation is the standard deviation of the logarithm of the flux values; it's also dimensionless.) The differences between these two measures can be seen in Figure 4: the geometric means (dots) are always to the left of the mean fluxes (vertical dashed lines), because values in the right-side tail of the distribution are exponentially larger than those in the left-side tail and contribute more to the mean flux. The non-linearity of the x-axis also means that an increase or decrease of the geometric standard deviation results in an increase or decrease, respectively, of the mean flux.

4.1 Explaining mean zonal momentum fluxes using the log-normal probability distribution

Motivated by the ubiquity of log-normal probability distributions in observed and modeled gravity wave momentum fluxes, in this section we use the distributions' properties to offer a statistical explanation for the sign and magnitude of the mean zonal momentum flux in each region. In some regions, like the Tropical and Extratropical Atlantic, it's clear from Figure 4 that the difference between the geometric means of the eastward and westward flux distributions contributes to the sign of the mean zonal momentum flux – one distribution is shifted relative to the other. In others, like the Southern Ocean, it's clear that the two distributions have different geometric standard deviations – one distribution is wider or narrower than the other. We quantify the contributions of the two statistical moments to the mean zonal momentum flux by separately shifting and squeezing the eastward and westward flux distributions so that either their geometric means or geometric standard deviations match, then record the resulting change in the mean

zonal flux. Four of these calculations are performed for each region: one matching the eastward flux distribution's geometric mean to the westward's, one to match the westward's to the eastward's, one to match the eastward flux distribution's geometric standard deviation to the westward's, and one to match the westward's to the eastward's. The average changes to the zonal momentum flux for changing the geometric mean and standard deviation, expressed as a percent of the mean zonal momentum flux, are given in Table 1.

For the sake of clarity, we will describe this shifting and squeezing procedure in more detail for an analysis of one region's momentum flux probability distributions. In the Tropical Atlantic, the geometric mean of the eastward momentum flux distribution is -0.09, and for the westward momentum flux distribution it's 0.10 (Table 2), a difference of 0.19. If we increase the values of the eastward momentum fluxes so that the logarithm of each of them is 0.19 higher, the mean eastward momentum flux increases by 0.76 mPa, from 1.37 mPa (Table 1) to 2.13 mPa. If we decrease the values of the westward momentum fluxes so that the logarithm of each of them is 0.19 lower, the mean westward momentum flux decreases by 0.78 mPa, from 2.19 mPa (Table 1) to 1.41 mPa. The average of these two changes expressed as a zonal momentum flux is 0.77 mPa, or 94 % of the mean zonal momentum flux of -0.82 mPa (Table 1; the percentage has the opposite sign as the ratio of the change to the mean zonal momentum flux). That is, 94% of the mean zonal momentum flux can be explained by the higher geometric mean of the westward momentum flux probability distribution. The percent of the mean zonal momentum flux that can be explained by the difference between the distributions' geometric standard deviations is calculated in the same way, by changing the values of one distribution's momentum fluxes so that the standard deviation of their logarithm matches the other distribution's geometric standard deviation. Changing the eastward momentum flux values in this way decreases the mean eastward momentum flux of 0.04 mPa, and its companion calculation increases the mean westward momentum flux by 0.09 mPa. The average of these two changes expressed as a zonal momentum flux is -0.07 mPa, or -8 % of the mean zonal momentum flux (Table 1). So, in the case of the Tropical Atlantic, the geometric means of the eastward and westward momentum flux probability distributions explain both the sign and magnitude of the mean zonal momentum flux, while their geometric standard deviations explain neither.

In five of the six regions, differences between the geometric means of the eastward and westward flux probability distributions explain a larger percentage of the mean zonal flux than differences between the distributions' geometric standard deviations. In four of those regions – the Tropical Atlantic, the Extratropical Pacific, the Extratropical Atlantic, and the Southern Ocean – the geometric means explain at least 75 % of the mean zonal momentum flux, while the geometric standard deviations explain at most 17 %. In the Tropical Pacific, the geometric standard deviations account for a larger percentage, 51 %, but the geometric means still explain more, 71 %. The only region where the percentage is higher for the geometric standard deviations than the geometric means is the Indian Ocean, by 55 to 48 %. Even in the Indian Ocean, though, the geometric means correctly explain the sign of the mean zonal momentum flux (its percentage is never negative for any region).

None of the regions' probability distributions are perfectly log-normal, so the two percentages never add up to exactly one hundred. For all six regions, though, they add up to within 25 % of one hundred, so both the sign and the magnitude of the mean zonal momentum flux can be explained using only the geometric means and geometric standard deviations of the momentum flux probability distributions. In four of the six regions, only the geometric means are necessary.

We come to the same conclusions when analyzing inter-regional differences of the mean zonal momentum flux. For example, 97% of the difference between the mean westward fluxes in the Tropical Atlantic (2.19 mPa) and Tropical Pacific (1.33 mPa) is due to the difference between the two distributions' geometric means (-1 % is due to their geometric standard deviations). These two regions have very similar mean eastward momentum fluxes, so the difference between their mean zonal momentum fluxes can now be attributed to the higher geometric mean of the Tropical Atlantic's westward momentum flux distribution. Comparing the Extratropical Atlantic to the Extratropical Pacific, 95 and 109 % of the difference between their mean eastward and westward momentum fluxes, respectively, is due to the difference between the distributions' geometric means (-5 % and -8 % is due to their geometric standard deviations). So, almost all of the difference in the mean zonal momentum flux between the two regions can be attributed to differences between their momentum flux distributions' geometric means.

4.2 Explaining 99th percentile fluxes and flux intermittencies

If momentum flux probability distributions' geometric means and geometric standard deviations can statistically explain differences between mean momentum fluxes, can they be used to account for differences between the distributions' tails as well? The right-side tails of the distributions are of particular interest, because large but infrequent momentum fluxes are known to be responsible for large fractions of the mean flux (another property of the log-normal distribution; Hertzog et al., 2012). Table 3 gives the 99th percentile fluxes for each region's eastward and westward momentum fluxes, as well as the percent of the mean flux due to fluxes above the 99th percentile. In general, both the 99th percentile flux and the percent of the total flux increase with the mean eastward and westward fluxes (Table 1); the largest values are in the Extratropical Atlantic and the Southern Ocean. We use the same distribution shifting/squeezing procedure described above to explain the east-west differences between the 99th percentile fluxes. Again, the distributions' geometric means more often explain a higher percent of the difference than the geometric standard deviations, with the exception again being the Indian Ocean. The difference between the 99th percentile fluxes in the Tropical Pacific is so small that the percentages are meaningless. It is worth noting that the two percentages only add up to within 25 % of one hundred in two regions this time, so this method is less accurate for explaining the distributions' tails than the mean momentum flux.

For a perfectly log-normal probability distribution, only the geometric standard deviation is needed to quantify the intermittency of the momentum flux. As in Hertzog et al. (2008), we define the intermittency as the ratio of the median to the 90th percentile momentum flux (note that, as the momentum flux becomes more intermittent, this measure of the intermittency goes down). More generally, the ratio of the median momentum flux to a value $M\sigma$ away from the median, where M is a positive real number and σ is the geometric standard deviation, is equal to $10^{-M\sigma}$ for a log-normal distribution. The value of M at the 90th percentile is approximately 1.3. This theoretical intermittency curve, along with the intermittency calculated from each region's probability distribution of the total momentum flux, is shown in Figure 5. While the regional values of the intermittency do not perfectly follow the theoretical curve, they do appear to have an exponential dependence on the geometric standard deviation, and the theoretical curve never overestimates the intermittency by more than 20 %. The four regions furthest from the theoretical curve all have flux probability distributions with positive kurtosis and skewness

relative to a log-normal distribution, elongating their right-side tails and reducing the value of the intermittency. In the Southern Ocean, one possible contributor to this is the choice of the geographic mask (Figure 3), which likely doesn't exclude some highly intermittent orographic waves generated by flow over the Andes mountains, waves which can propagate eastward and southward over the ocean (Kruse et al., 2022).

5 Dependence of the mean zonal momentum flux on the background zonal wind

The balloon data also contain information about the environment the waves propagate in; namely, the "background" wind. Estimating the background wind from atmospheric reanalysis, Plougonven et al. (2017) showed the total gravity wave momentum flux above Antarctica and the high-latitude Southern Ocean increases with the background wind speed. Following on from their results, in this section we study the dependence of the zonal momentum flux on the strength of the background zonal wind.

We calculate the background zonal wind by smoothing the zonal wind time series using a Gaussian filter with a half-width set to the maximum gravity wave period in our analysis, either the Coriolis period or one day, whichever is smaller. This filter width effectively eliminates inertial oscillations, while still allowing for the smoothed wind time series to vary over the length of a two-day segment. Figure 6 shows the probability densities of the smoothed zonal wind in each region. In the Extratropical Pacific, the mean smoothed zonal wind is easterly, which likely results from a bias in the balloons' sampling of that region. In the other two mid-latitude regions, the mean smoothed zonal wind is westerly, and in the Southern Ocean it has a wide range of values, from weakly easterly to above 60 m/s westerly. There also appears to be a sampling bias in the Tropical Atlantic, where the mean wind is more westerly than the other two tropical regions.

There is an order of magnitude more data in the Southern Ocean than in the other regions, and since the range of values of the smoothed zonal wind is larger there, too, it's the region best suited for studying the relationship between zonal momentum fluxes and the smoothed zonal wind. Figure 7 shows probability distributions of the eastward and westward momentum fluxes when the flux values are binned into three ranges of their concurrent smoothed zonal wind values: 0-20, 20-40, and 40-60 m/s. As the wind strength increases, the means of both the eastward and westward momentum fluxes also increase. The mean westward momentum flux outpaces the eastward, so the mean zonal momentum flux becomes more negative as the winds become more westerly, increasing in magnitude from -0.45 to -2.90 to -4.05 mPa. The mean zonal wind and zonal momentum flux in Southern Ocean data is 21 m/s and -1.64 mPa (Table 1), consistent with this relationship.

Plougonven et al. (2017) found that, as the wind speed increases, the geometric mean of the momentum flux distribution also increases, but the geometric standard deviation remains relatively constant (see their Figure 8). Our results are consistent with theirs: for the data in the Southern Ocean, the increases of the geometric means from the weakest to the strongest wind band are larger than any changes of the geometric standard deviations (Table 2). As might be obvious from Figure 7, the distributions' geometric means explain much more of the differences between the mean fluxes than their geometric standard deviations do. Using the method described in section 4.1, we find that more than 80 % of the difference between mean fluxes is explained by the distributions' geometric means, whether the comparison is between the

eastward and westward fluxes in a given wind band, or between the eastward or westward fluxes across wind bands.

Though there are fewer data in the other five regions and the distributions of their smoothed zonal winds aren't as broad, their mean momentum fluxes also show a dependence on the background wind speed. For both the Extratropical Atlantic and Extratropical Pacific, we compare the mean momentum fluxes in two bands of the smoothed zonal wind, one weak wind band and one strong wind band, defined based on the probability distributions in Figure 6. The weak wind band is always between -5 and 5 m/s; the strong wind band is between -15 and -5 m/s in the Extratropical Pacific and between 5 and 15 m/s in the Extratropical Atlantic. As in the Southern Ocean, the mean zonal momentum flux becomes stronger in the direction opposite the wind as the wind becomes stronger. The mean zonal momentum flux in the Extratropical Pacific in the weak wind band is -0.03 mPa, and in the strong wind band it is 0.55 mPa. In the Extratropical Atlantic it's -0.85 mPa in the weak wind band and -1.17 mPa in the strong wind band. Again like in the Southern Ocean, the magnitudes of both the mean eastward and mean westward momentum fluxes increase with the wind speed in both regions (not shown).

It is worth noting that the negative mean zonal momentum flux in the Extratropical Pacific can now be explained as resulting from a possible bias in the balloon sampling of that region – in general, we would expect the zonal wind in that region to be westerly, which we now anticipate would result in a positive mean zonal momentum flux. As shown in Figure 3, most of the data in the Extratropical Pacific come from 2014, so it's possible interannual variability contributed to the mean easterly zonal wind. Seasonal sampling bias doesn't seem to significantly contribute: only 27 % of the data come from June, July, and August, and summer is the only season when the climatological winds in the northern hemisphere extratropical lower stratosphere are easterly. Other sources of sampling biases, such as the balloons sampling local conditions unrepresentative of the zonal mean climatology, are possible.

In the three tropical regions the natural choice is to compare the momentum fluxes when the background wind is easterly to when it is westerly. In both the Indian Ocean and Tropical Pacific, the sign of the mean zonal momentum is opposite the sign of the smoothed zonal wind, but in the Tropical Atlantic, this isn't always the case. When the background wind is westerly, the mean zonal fluxes in the Indian Ocean, Tropical Pacific, and Tropical Atlantic are -0.15, -0.21, and -0.93 mPa, respectively. When the background wind is easterly, the fluxes are 0.61, 0.24, and -0.33 mPa, respectively. Figure 6 shows that there are relatively few observations of easterly winds in the Tropical Atlantic, the region that also has the fewest number of total observations, so the -0.33 mPa value should be treated with some skepticism. This sampling bias likely contributes to the negative mean zonal momentum flux in the Tropical Atlantic (Table 1).

6 Momentum fluxes by high-, medium-, and low-frequency waves

So far, we have presented momentum fluxes that have been integrated across the gravity wave frequency spectrum. The frequency spectrum of the gravity wave momentum flux has an approximate ω^{-1} dependence (Hertzog et al., 2008) in the mean, but how variable is this relationship? In this section we analyze the contributions by high-, medium-, and low-frequency waves to the varying magnitude of the momentum flux.

To separate the momentum flux into contributions by those three wave types, we divide the wavelet cross-spectra into three bands between the minimum and maximum wave

526 frequencies, then integrate in frequency to create momentum flux time series for each band. The
527 frequencies separating the three bands for the data segment shown in Figure 1 are the dashed
528 lines in Figure 1b and are chosen so the bands have equal width in the logarithm of frequency.
529 This choice was made partially out of convenience – as we'll show, the momentum fluxes in the
530 three bands have similar magnitudes – and partially to separate waves based on the magnitudes
531 of their intrinsic frequencies, since the magnitude of the intrinsic frequency can be used to make
532 helpful simplifications to the gravity wave dispersion relation (see sections 2.1.1-3 of Fritts and
533 Alexander, 2003). For a balloon flying at the equator, the three bands cover wave periods
534 between 10 and 52 minutes, 52 minutes and 4.6 hours, and 4.6 and 24 hours. If the balloon was
535 flying at 45 °S, the three period ranges would be 10 to 47 minutes, 47 minutes to 3.6 hours, and
536 3.6 to 17 hours. In our analysis, we let the period range vary over the course of a balloon flight.
537 Figure 8 shows how the percent contributions of high-, medium-, and low-frequency
538 waves to the total zonal and meridional momentum fluxes changes with the magnitude of the
539 total flux. By "total," we mean the sum of, not the difference between, the directional fluxes: the
540 total zonal flux is the sum of the eastward and westward fluxes, and the total meridional flux is
541 the sum of the northward and southward fluxes. In every region, and for both the zonal and
542 meridional fluxes, the percent contribution by high frequency waves to the total flux increases
543 with the magnitude of the flux. Conversely, the contribution by low frequency waves to the total
544 fluxes everywhere decreases with the magnitude of the flux. The cross-over point where the
545 high-frequency waves contribute more to the total flux than the low-frequency waves do is
546 typically between 5 and 10 mPa. If we compare the contributions by the three wave types to the
547 pseudo-momentum flux, the contribution by low-frequency waves reduces by as much a 10 % in
548 the three extratropical regions, and the cross-over point increases by a couple millipascals, but
549 the shapes of the curves are unchanged (not shown).
550 The cause of the relationships in Figure 8 is unclear, but they are robust to the choices we
551 made in our analysis. If we fix the period ranges defining the three wave types (to 10 to 50
552 minutes, 50 minutes to 4 hours, and 4 hours to 1 day or the Coriolis period), the contribution by
553 the high frequency waves to the total flux still increases with the magnitude of the total flux, and
554 the contribution by the low frequency waves still decreases (not shown). Figure 1 implies that,
555 when the total momentum flux is low, many of the wavelet coefficients in the high-frequency
556 band are deleted because they do not meet the noise threshold. If we eliminate the noise
557 threshold criteria and retain all wavelet coefficients regardless of their magnitude, the fraction of
558 the total fluxes due to the high frequency waves increases, but the increase is only noticeable at
559 total flux magnitudes below 2 mPa or so (not shown). Below 2 mPa, the high-, medium-, and
560 low-frequency curves become approximately flat. Finally, though our analyses have focused on
561 waves over the oceans, if we perform the same frequency-band decomposition on data from all
562 regions not colored in in Figure 3, we see the same trends in the high- and low-frequency
563 momentum fluxes ("All Other Data," Figure 8). This result includes all the data collected over
564 land, indicating that, in this respect, non-orographic and orographic gravity waves behave
565 similarly.
566 Combined with the results in Tables 1 and 3, Figure 8 offers a time-dependent
567 interpretation of the approximately ω^{-1} dependence of the gravity wave momentum flux
568 spectrum mentioned earlier. At most times and in most places in the lower stratosphere, the
569 gravity wave momentum flux has a magnitude on the order of 1 mPa, and low-frequency waves
570 contribute the most to the flux and high-frequency waves contribute the least. The time-mean
571 momentum flux frequency spectrum reflects these conditions. Less than 1% of the time,

however, the momentum flux has an amplitude on the order of 10 mPa or higher, most of which is attributed to high-frequency waves, and the momentum flux frequency spectrum momentarily has a shallower slope. Also rarely, the amplitude of the momentum flux is much smaller than 1 mPa; the slope then is steeper.

7 Summary and discussion

Our aim in this paper has been to estimate and build a consistent statistical description of gravity wave momentum fluxes from Project Loon balloon data, starting with mean momentum fluxes, then describing their probability distributions, then studying the dependence of the momentum flux on the background wind and the wave frequency. The maps of mean momentum fluxes presented in Figure 2 show large-scale patterns in the zonal flux, with largely westward fluxes in the mid-latitudes and a mix of easterly and westerly fluxes in the tropics. Liu et al. (2022) studied tropical momentum fluxes by coupling a gravity wave parameterization to winds from atmospheric reanalysis and convective latent heating profiles derived from observations and obtained an eastward mean zonal momentum flux near the equator in the tropical tropopause layer (see their Figure 6). While we found large regions of eastward momentum fluxes near the equator in the Tropical Pacific and Indian Oceans, the mean zonal momentum flux in the Tropical Atlantic is westward. That mean zonal flux, though, is the result of a cancellation between larger mean eastward and westward fluxes (Table 1) and is likely affected by sampling biases. More observations would be needed to comment further on Liu et al.'s result.

We found in section 4 that basic properties of the momentum flux probability distribution have significant power to explain aspects of both the spatial and temporal variability of the non-orographic gravity wave momentum flux. It is well-known that gravity wave momentum fluxes are distributed approximately log-normally; we found that the first two moments of their probability distributions contain enough information to statistically explain the sign and magnitude of the mean momentum flux and the momentum flux intermittency in all six geographic regions we studied, and the 99^{th} percentile momentum fluxes in some regions. In four of the six regions identified in Figure 3 – the Tropical Atlantic, the Extratropical Atlantic, the Extratropical Pacific, and the Southern Ocean – the difference between the eastward and westward momentum flux distributions' geometric means explains more than 75 % of the mean zonal flux (Table 1). They account for almost all of the inter-regional differences in the mean eastward and westward fluxes between the Extratropical Atlantic and Extratropical Pacific. Though the geometric standard deviation has more skill explaining the magnitude of the mean zonal flux in the Indian Ocean, the geometric mean still correctly explains its sign there and in the Tropical Pacific. We suggest the simplest statistical interpretation of the mean zonal momentum flux is the difference that results when otherwise identical log-normal eastward and westward momentum flux probability distributions are shifted relative to each other along the axis of the logarithm of the momentum flux.

We also found that both the magnitude of the momentum flux intermittency and its difference between regions are closely related to the geometric standard deviation of the momentum flux probability distribution. None of the six regions' distributions are perfectly log-normal, but Figure 5 shows that the momentum flux intermittency nonetheless has an approximately exponential dependence on the geometric standard deviation. In five regions the

log-normal distribution slightly underestimates the intermittency metric, meaning it underpredicts the frequency of occurrence of (relatively) large magnitude momentum fluxes.

In section 5 we analyzed the dependence of the zonal momentum flux on the smoothed zonal wind. In the three mid-latitude regions our results agreed with Plougonven et al. (2017): the magnitude of the momentum flux increases with the strength of the wind. Mean zonal momentum fluxes become stronger in the direction opposite the wind, and the negative mean zonal flux measured in the Extratropical Pacific is likely the result of sampling biases there. We also found indications of sampling biases in the Tropical Atlantic. In the other two tropical regions, the mean zonal momentum flux is westward when the smoothed zonal wind is westerly and eastward when the wind is easterly. Figure 3 shows that Loon balloons flew near the equator more or less continuously from 2014 to 2021, so it's possible there are enough data to study the dependence of the gravity wave momentum flux on the Quasi-Biennial Oscillation.

The large range of zonal wind values in the data over the Southern Ocean indicate a connection between wave sources and the background wind, but the relative importance of wave filtering remains unclear. If the gravity wave source spectrum and filtering were fixed, a more westerly background wind at the balloon level would result in a decrease in both the number of waves propagating eastward relative to the balloon and the mean eastward momentum flux. (Concurrently, there would be an increase in the number of westward-propagating waves and the mean westward momentum flux.) However, Figure 7 shows that the mean eastward momentum flux increases with the background zonal wind, which if the wave sources remain fixed would require a significant reduction of the filtering of eastward-propagating waves, enough to more than offset the effect of the change in the background wind. This seems unlikely, since the range of background wind speeds is so large. More likely is either a broadening of the gravity wave phase speed source spectrum or an increase in the number or amplitude of sources of waves propagating eastward relative to the background flow. This change of wave sources with the background flow is likely also accompanied by changes in wave filtering, but our analysis is unable to determine the relative importance of the two.

How might our results be used to evaluate climate model or gravity wave parameterization output, or be used to improve or develop new parameterizations? First, they show that, ideally, a parameterization or high-resolution model should reproduce the log-normal shape of the momentum flux probability distribution in the lower stratosphere. Second, they provide constraints on the shape of that distribution – Table 2 shows that, from region to region and as the speed of the background wind varies, the geometric standard deviation varies less than the geometric mean. The relatively small variations in the geometric standard deviation are still important, though, since they affect the intermittency. Both statistical moments affect the magnitude and shape of the drag profile: the geometric mean its magnitude, primarily, and the geometric standard deviation its width, since stronger waves from a more intermittent source will break lower in the atmosphere (Bühler, 2003; Piani et al., 2004). Finally, section 6 showed why models that resolve only part of the gravity wave spectrum might not produce realistic gravity wave intermittencies. Figure 8 shows that the most intermittent waves – those with the largest amplitudes and momentum fluxes – are predominantly high-frequency waves. If models do not resolve these waves, their momentum flux probability distributions and drag profiles will likely be too narrow.

Many questions remain about gravity wave momentum fluxes and their probability distributions, some of which could be addressed by further analysis of the Loon balloon data. Are there any physical constraints on the range of the momentum flux probability distributions'

geometric means and standard deviations? Why does the mean momentum flux seem more sensitive to the geometric mean than the geometric standard deviation? For that matter, why are the distributions log-normal to begin with? One possible explanation is the critical-level filtering of a broad spectrum of gravity waves by a stochastic background wind field (Hertzog et al., 2012), and another is that the probability distribution of the wave sources is itself log-normal (de la Camara et al., 2014). It might be possible to discriminate between these two hypotheses in the Loon data by decomposing the momentum flux distributions into contributions by different wave sources, by estimating the waves' phase speeds and wavelengths, as in Boccara et al. (2008) and Vincent and Hertzog (2014). Relating the momentum fluxes to the phase speeds could also provide a helpful observational constraint on a relationship that is commonly used in parameterizations (e.g., Alexander and Dunkerton, 1999).

Acknowledgements

We thank Chris Kruse, Riwal Plougonven, Aurelien Podglajen, and Albert Hertzog for helpful discussions. This research was made possible by Schmidt Futures, a philanthropic initiative founded by Eric and Wendy Schmidt, as part of the Virtual Earth System Research Institute (VESRI). A.S. and B.G. acknowledge support from the National Science Foundation through grant OAC-2004492, and from Google LLC. M.J.A. and M.B. were supported by the National Science Foundation grant number 2004512, as well as grant numbers 1642644 and 1642246.

Open Research

COSMIC-1 data are available at: https://doi.org/10.5065/ZD80-KD74. COSMIC-2 data are available at: https://doi.org/10.5065/t353-c093. Loon data are available at: https://doi.org/10.5281/zenodo.5119968. Our data processing code, analysis code, and the estimated Loon gravity wave momentum fluxes are available at: https://drive.google.com/drive/folders/1LZT7bxeHMDt7dhv1ZL2oZCwch4Fc9Fcz?usp=sharing . Should this manuscript be accepted for publication, the final versions of these files will be uploaded to more permanent repositories.

References

Alexander, M., & Dunkerton, T. (1999). A spectral parametrization of mean-flow forcing due to breaking gravity waves. *Journal of the Atmospheric Sciences, 56,* 4167–4182. https://doi.org/10.1175/1520-0469(1999)056<4167:ASPOMF>2.0.CO;2

Alexander, M.J., Geller, M., McLandress, C., Polavarapu, S., Preusse, P., Sassi, F., et al. (2010). Recent developments in gravity-wave effects in climate models and the global distribution of gravity-wave momentum flux from observations and models. *Quarterly Journal of the Royal Meteorological Society, 136,* 1103-1124. https://doi.org/10.1002/qj.637

Anthes, R.A., Bernhardt, P.A., Chen, Y., Cucurull, L., Dymond, K.F., Ector, D., et al. (2008). The COSMIC/FORMOSAT-3 mission: Early results. *Bulletin of the American Meteorological Society, 89,* 313–333. https://doi.org/10.1175/BAMS-89-3-313

Boccara, G., Hertzog, A., Vincent, R.A., & Vial, F. (2008). Estimation of gravity wave momentum flux and phase speeds from quasi-Lagrangian stratospheric balloon flights. Part I: Theory and simulations. *Journal of the Atmospheric Sciences, 65,* 3042-3055. https://doi.org/10.1175/2008JAS2709.1

Bühler, O. (2003). Equatorward propagation of inertia–gravity waves due to steady and intermittent wave sources. *Journal of the Atmospheric Sciences, 60,* 1410–1419. https://doi.org/10.1175/1520-0469(2003)060<1410:EPOIWD>2.0.CO;2

de la Cámara, A., Lott, F., & Hertzog, A. (2014). Intermittency in a stochastic parameterization of nonorographic gravity waves. *Journal of Geophysical Research: Atmospheres, 119,* 11,905-11,919. https://doi.org/10.1002/2014JD022002

Conway, J.P., Bodeker, G.E., Waugh, D.W., Murphy, D.J., Cameron, C., & Lewis, J. (2019). Using Project Loon superpressure balloon observations to investigate the inertial peak in the intrinsic wind spectrum in the midlatitude stratosphere. *Journal of Geophysical Research: Atmospheres, 124,* 8594-8604. https://doi.org/10.1029/2018JD030195

Corcos, M., Hertzog, A., Plougonven, R., & Podglajen, A. (2021). Observation of gravity waves at the tropical tropopause using superpressure balloons. *Journal of Geophysical Research: Atmospheres, 126,* e2021JD035165. https://doi.org/10.1029/2021JD035165

Fritts, D.C., & Alexander, M.J. (2003). Gravity wave dynamics and effects in the middle atmosphere. *Reviews of Geophysics, 41(1),* 1003. https://doi.org/10.1029/2001RG000106

Fritts, D.C., & Alexander, M.J. (2012). Correction to "Gravity wave dynamics and effects in the middle atmosphere." *Reviews of Geophysics, 50,* RG3004. https://doi.org/10.1029/2012RG000409

Hertzog, A., Alexander, M.J., & Plougonven, R. (2012). On the intermittency of gravity wave momentum flux in the stratosphere. *Journal of the Atmospheric Sciences, 69,* 3433-3448. https://doi.org/10.1175/JAS-D-12-09.1

Hertzog, A., Boccara, G., Vincent, R.A., Vial, F., & Cocquerez, P. (2008). Estimation of gravity wave momentum flux and phase speeds from quasi-Lagrangian stratospheric balloon flights. Part II: Results from the Vocore campaign in Antarctica. *Journal of the Atmospheric Sciences, 65,* 3056-3070. https://doi.org/10.1175/2008JAS2710.1

Hertzog, A., Cocquerez, P., Basdevant, C., Boccara, G., Bordereau, J., Briott, B., et al. (2007). Stratéole/Vorcore—long-duration, superpressure balloons to study the Antarctic lower stratosphere during the 2005 winter. *Journal of Atmospheric and Oceanic Technology, 24,* 2048-2061. https://doi.org/10.1175/2007JTECHA948.1

Jewtoukoff, V., Hertzog, A., Plougonven, R., de la Camara, A., & Lott, F. (2015). Comparison of gravity waves in the Southern Hemisphere derived from balloon observations and the ECMWF analyses. *Journal of the Atmospheric Sciences, 72,* 3449-3468. https://doi.org/10.1175/JAS-D-14-0324.1

Kruse, C. G., Alexander, M. J., Hoffmann, L., Niekerk, A. V., Polichtchouk, I., Bacmeister, J. T., et al. (2022). Observed and modeled mountain waves from the surface to the mesosphere near the drake passage. *Journal of the Atmospheric Sciences*, *79*, 909–932. https://doi.org/10.1175/JAS-D-21-0252.1

Lilly, D.K., & Kennedy, P.J. (1973). Observations of a stationary mountain wave and its associated momentum flux and energy dissipation. *Journal of the Atmospheric Sciences, 30,* 1135-1152. https://doi.org/10.1175/1520-0469(1973)030<1135:OOASMW>2.0.CO;2

Lindgren, E.A., Sheshadri, A., Podglajen, A., & Carver, R.W. (2020). Seasonal and latitudinal variability of the gravity wave spectrum in the lower stratosphere. *Journal of Geophysical Research: Atmospheres*, *125*, e2020JD032850. https://doi.org/ 10.1029/2020JD032850

Liu, C., Alexander, J., Richter, J., & Bacmeister, J. (2022). Using TRMM latent heat as a source to estimate convection induced gravity wave momentum flux in the lower stratosphere. *Journal of Geophysical Research: Atmospheres*, *127,* e2021JD035785. https://doi.org/10.1029/2021JD035785

Lott, F. (1995). Comparison between the orographic response of the ECMWF model and the PYREX 1990 data. *Quarterly Journal of the Royal Meteorological Society, 121,* 1323-1348. https://doi.org/10.1002/qj.49712152607

Lott, F., Rani, R., Podglajen, A., Codron, F., Guez, L., Hertzog, A., & Plougonven, R. (2023). Direct comparison between a non-orographic gravity wave drag scheme and constant level balloons. *Journal of Geophysical Research: Atmospheres*, *128,* e2022JD037585. https://doi.org/10.1029/2022JD037585

Piani, C., Norton, W. A., & Stainforth, D. A. (2004). Equatorial stratospheric response to variations in deterministic and stochastic gravity wave parameterizations. *Journal of Geophysical Research*, *109*, D14101. https://doi.org/10.1029/2004JD004656

Plougonven, R., de la Camara, A., Hertzog, A., & Lott, F. (2020). How does knowledge of atmospheric gravity waves guide their parameterizations? *Quarterly Journal of the Royal Meteorological Society, 146,* 1529-1543. https://doi.org/10.1002/qj.3732

Plougonven, R., Jewtoukoff, V., de la Camara, A., Lott, F., & Hertzog, A. (2017). On the relation between gravity waves and wind speed in the lower stratosphere over the Southern Ocean. *Journal of the Atmospheric Sciences, 74,* 1075-1093. https://doi.org/10.1175/JAS-D-16-0096.1

Podglajen, A., Hertzog, A., Plougonven, R., & Legras, B. (2016). Lagrangian temperature and vertical velocity fluctuations due to gravity waves in the lower stratosphere. *Geophysical Research Letters, 43,* 3543–3553. https://doi.org/10.1002/2016GL068148

Rabier, F., Bouchard., A., Brun, E., Doerenbecher, A., Guedj, S., Guidard, V., et al. (2010). The Concordiasi project in Antarctica. *Bulletin of the American Meteorological Society, 91(1),* 69-86. https://doi.org/10.1175/2009BAMS2764.1

Rhodes, B. & Candido, S. (2021). Loon stratospheric sensor data (Version 3) [Dataset]. Zenodo. https://doi.org/10.5281/zenodo.5119968

Schoeberl, M.R., Jensen, E., Podglajen, A., Coy, L., Lodha, C., Candido, S., & Carver, R. (2017). Gravity wave spectra in the lower stratosphere diagnosed from project loon balloon trajectories. *Journal of Geophysical Research: Atmospheres, 122,* 8517-8524. https://doi.org/10.1002/2017JD026471

Smith, R.B., Nuget, A.D., Kruse, C.G., Fritts, D.C., Doyle, J.D., Eckermann, S.D., et al. (2016). Stratospheric gravity wave fluxes and scales during DEEPWAVE. *Journal of the Atmospheric Sciences, 73,* 2851-2869. https://doi.org/10.1175/JAS-D-15-0324.1

Torrence, C., & Compo, G.P. (1998). A practical guide to wavelet analysis. *Bulletin of the American Meteorological Society, 79(1),* 61-78. https://doi.org/10.1175/1520-0477(1998)079<0061:APGTWA>2.0.CO;2

Vincent, R.A., & Alexander, M.J. (2020). Balloon-borne observations of short vertical wavelength gravity waves and interaction with QBO winds. *Journal of Geophysical Research: Atmospheres, 125,* e2020JD032779. https://doi.org/10.1029/2020JD032779

Vincent, R.A., & Hertzog, A. (2014). The response of superpressure balloons to gravity wave motions. *Atmospheric Measurement Techniques, 7(4),* 1043–1055. https://doi.org/10.5194/amt-7-1043-2014

Yue, X., W.S. Schreiner, N. Pedatella, R.A. Anthes, A.J. Mannucci, P.R. Straus, & J.-Y. Liu (2014). Space Weather Observations by GNSS Radio Occultation: From FORMOSAT-3/COSMIC to FORMOSAT-7/COSMIC-2. *Space Weather, 12,* 616–621. https://doi.org/10.1002/2014SW001133

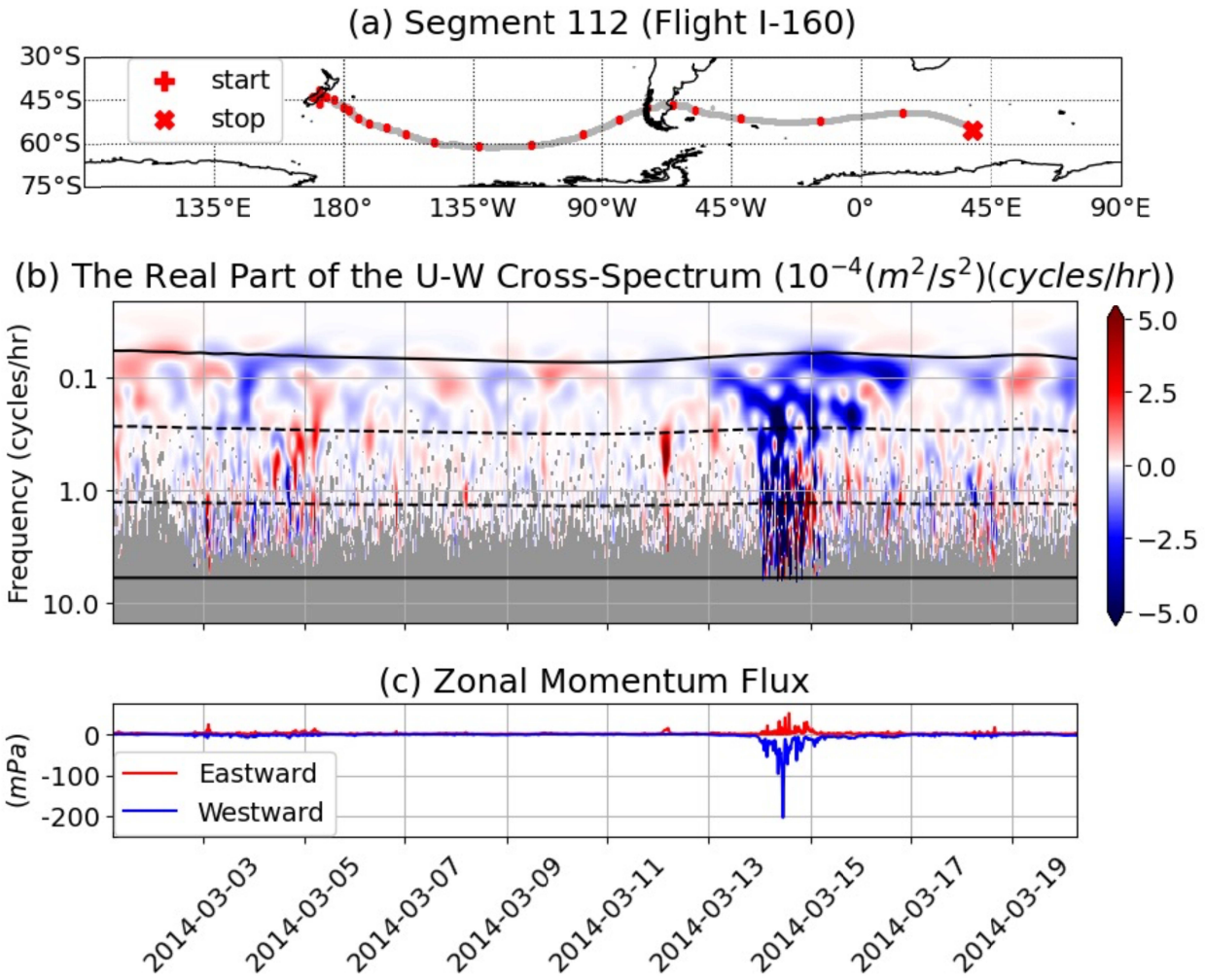

Figure 1. Sample analysis of a balloon data segment. (a) The flight path of the balloon, with red dots spaced one day apart. (b) The wavelet cross-spectrum of the zonal and vertical wind anomalies, times the wavelet frequency. Solid black lines indicate the minimum and maximum GW frequencies of 1/(10 minutes) and the Coriolis frequency. Dashed lines indicate the cutoff frequencies separating the high-, medium-, and low-frequency waves described in Section 6. At a given time and frequency, if either the *u* or *w* amplitude is less than three times the instrumental uncertainty, the cross-spectrum wavelet coefficient is colored gray. (c) GW momentum flux time series, calculated by integrating the positive and negative wavelet cross-spectrum coefficients separately. Note that everywhere else the eastward and westward momentum fluxes are defined as positive-definite, and the zonal momentum flux is their difference.

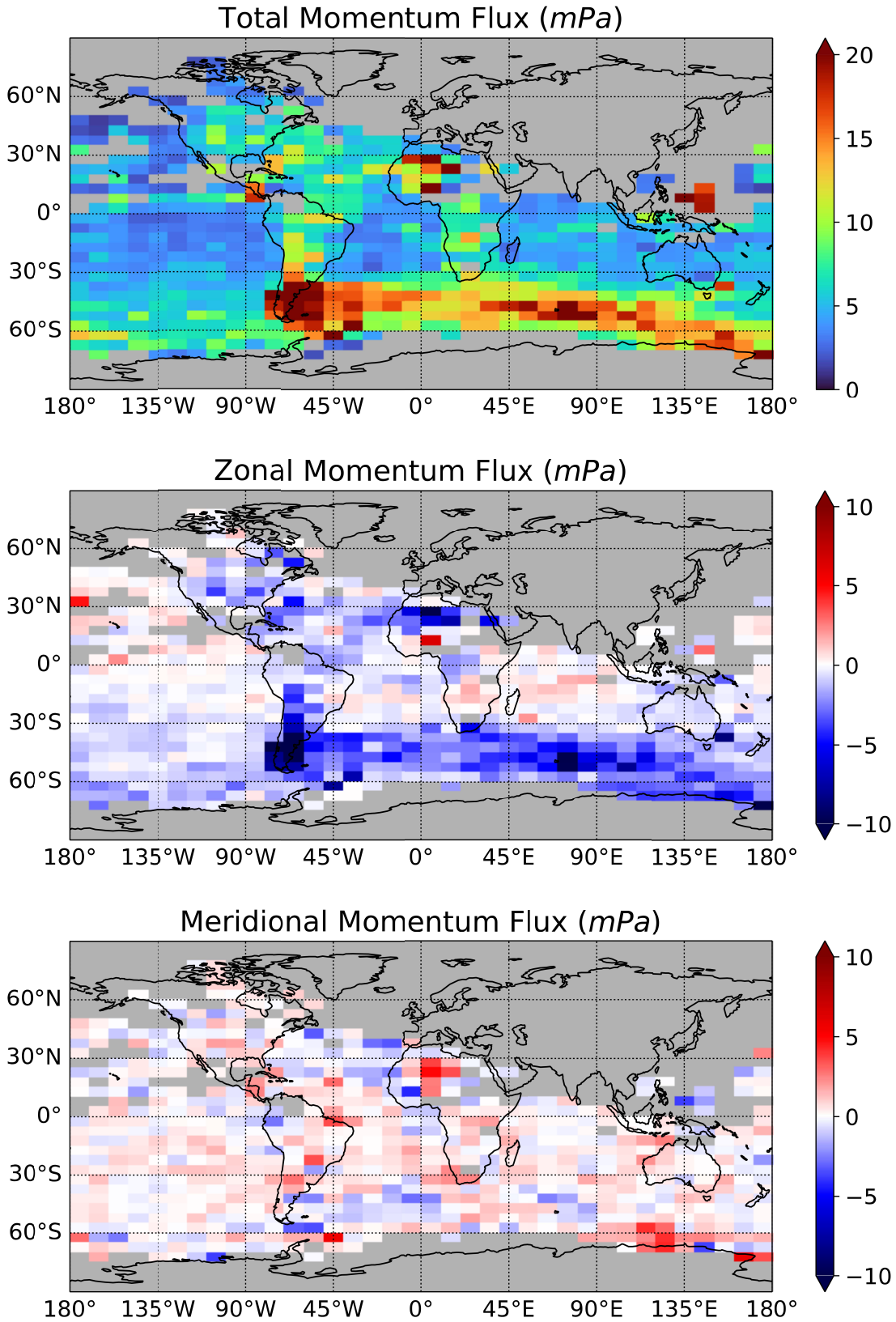

Figure 2. The mean GW momentum fluxes measured inside 5° latitude by 10° longitude grid cells. Grid cells with fewer than 500 data points are colored gray. The total momentum flux is

the square root of the sum of the squared total zonal (eastward + westward) and total meridional (northward + southward) momentum fluxes.

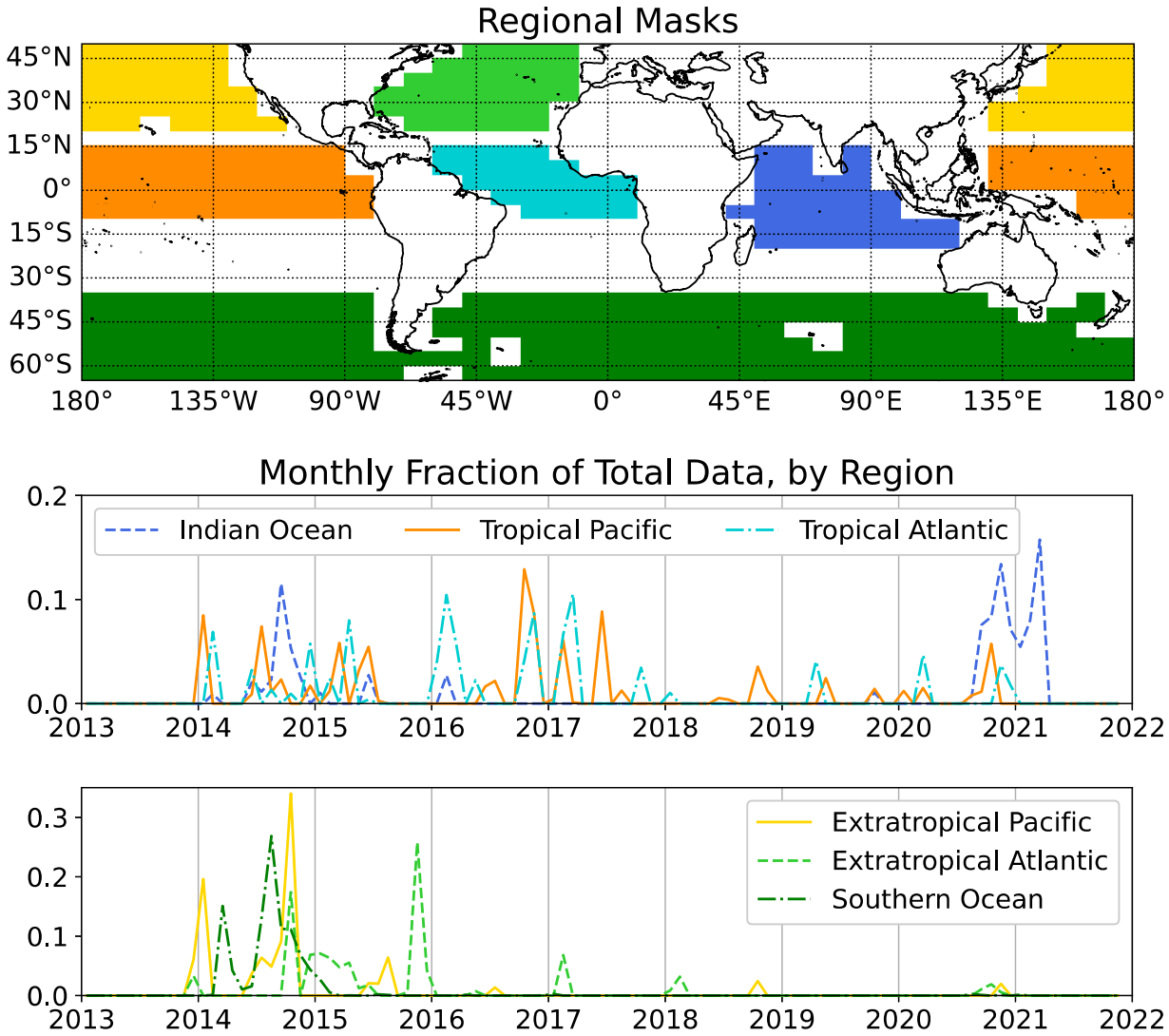

Figure 3. Regional data masks. Top: data collected inside each colored region is assigned to that region. Middle, bottom: the monthly fraction of the total data collected in each region.

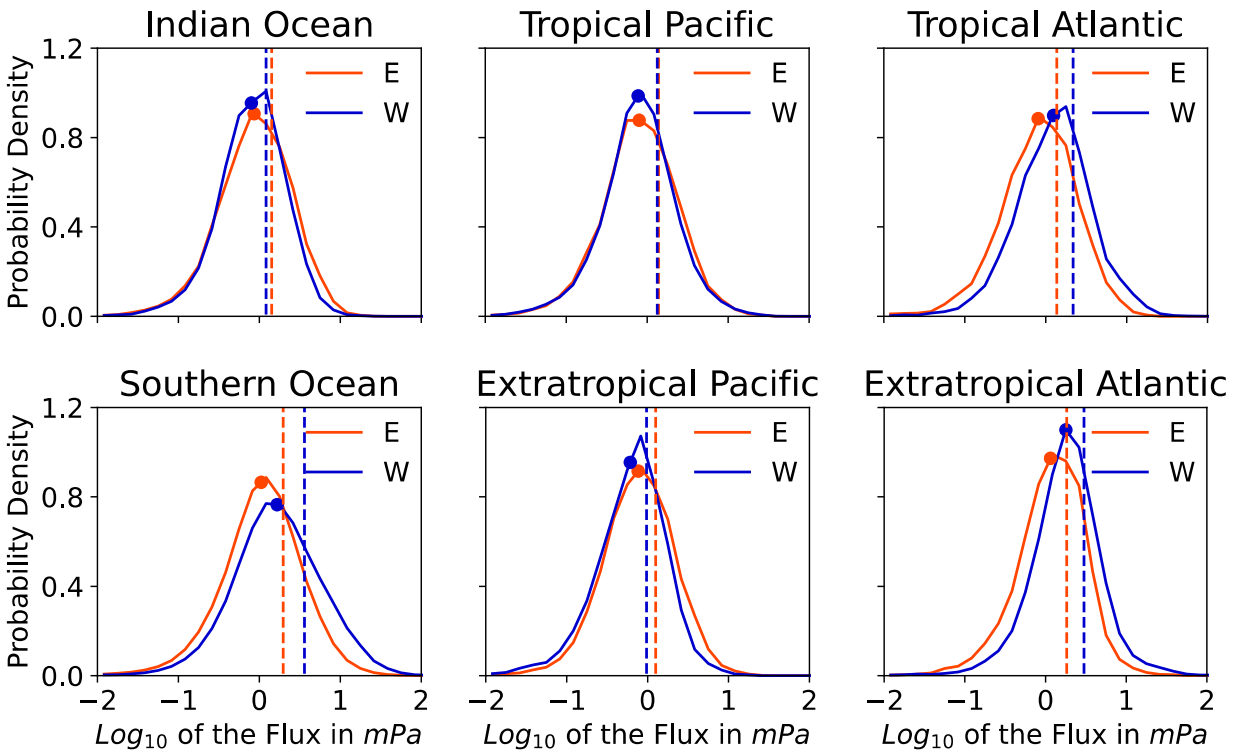

Figure 4. Probability densities of the eastward (E) and westward (W) momentum fluxes in each region. To calculate the distributions, we use 30 bins evenly spaced in log_{10} of the momentum flux, from -2 to 3 (10^{-2} to 10^{3} mPa). The vertical dashed lines are the logarithm of the mean momentum fluxes from Table 1. Dots indicate the distributions' geometric means.

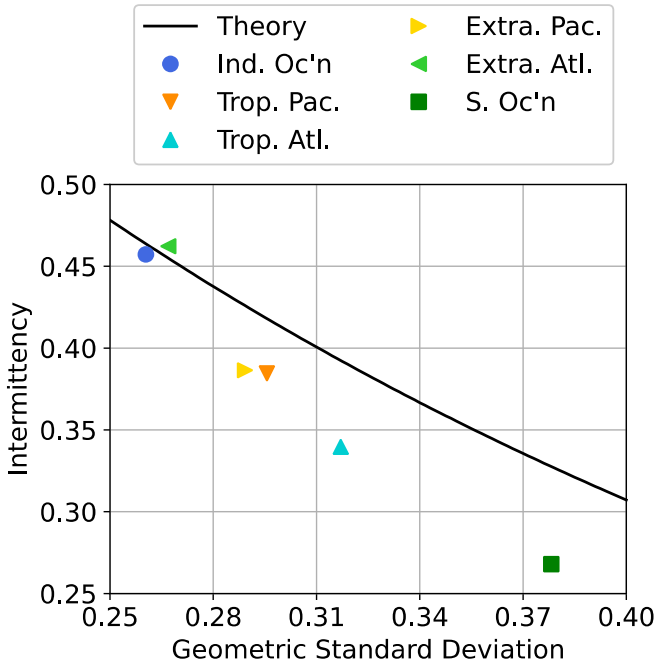

Figure 5. Statistics of the probability distribution of the total momentum flux, by region.

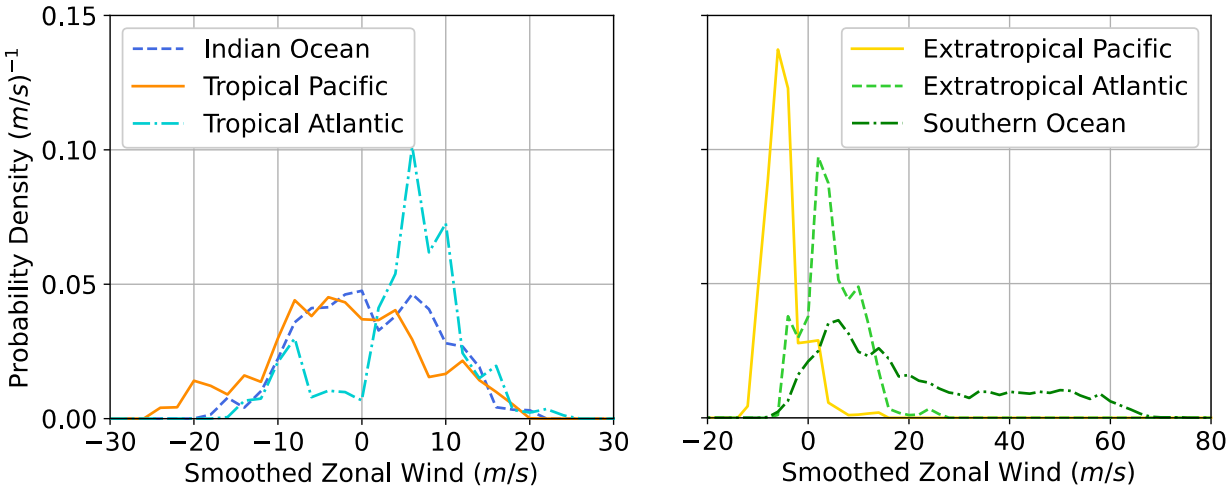

Figure 6. Probability densities of the smoothed zonal wind in each region. To calculate the distributions, we use 2 m/s-wide bins.

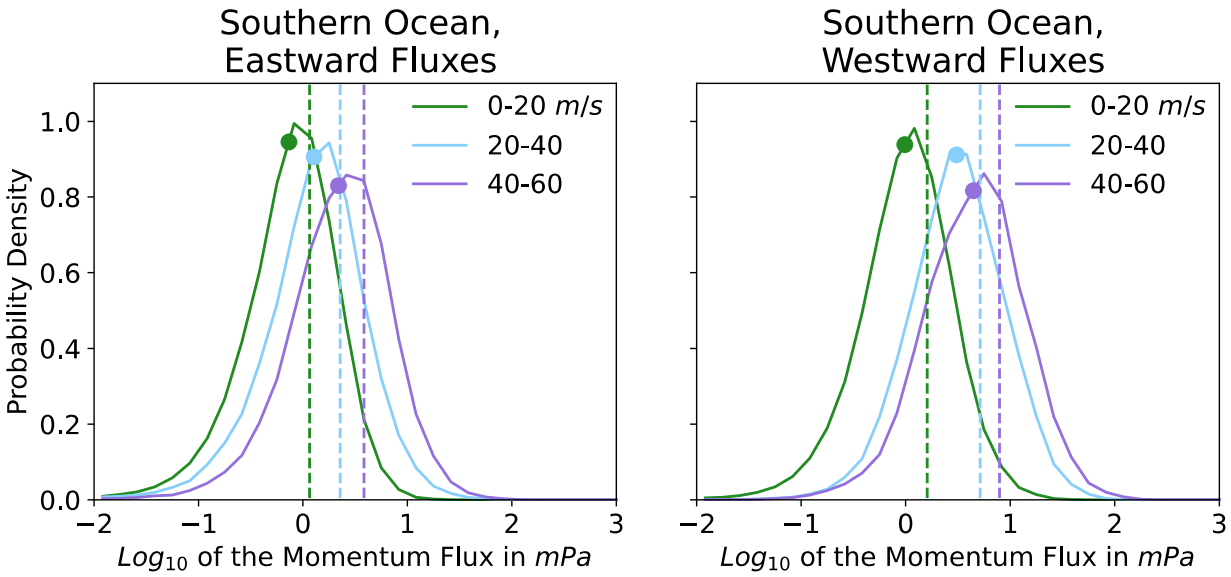

Figure 7. Probability densities of the eastward and westward momentum fluxes in the Southern Ocean, classified by the velocity of the smoothed zonal wind. The bin resolution is the same as in Figure 4. The mean eastward momentum flux in the 0-20, 20-40, and 40-60 m/s smoothed zonal wind ranges are 1.16, 2.27, and 3.85 mPa, respectively (dashed lines, left panel). The mean westward momentum flux in the 0-20, 20-40, and 40-60 m/s smoothed zonal wind ranges are 1.61, 5.17, and 7.90 mPa, respectively (dashed lines, right panel). Dots indicate the distributions' geometric means.

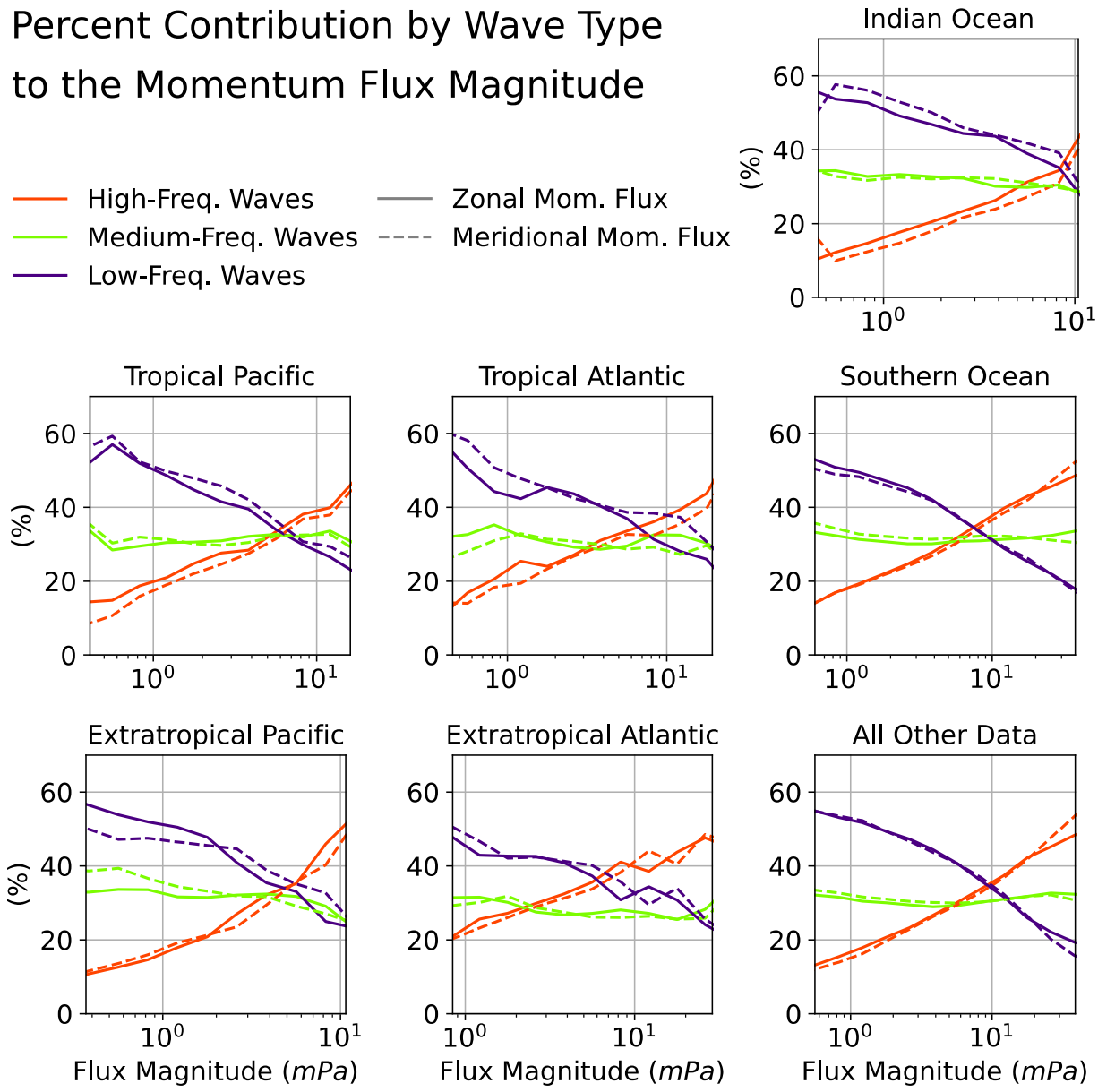

Figure 8. The fraction of the magnitude of the zonal (solid lines) and meridional (dashed lines) momentum fluxes due to high-, medium-, and low-frequency waves. The flux magnitudes are calculated by setting all component (northward, southward, eastward, and westward) flux time series to be positive and taking their sum, eastward + westward in the zonal direction, and northward + southward in the meridional direction. This is equivalent to taking the absolute value of the wavelet coefficients in Figure 1. We then bin the data by the flux magnitude for each region and calculate the average percent of that flux contributed by waves in each frequency band. The "All Other Data" region represents all the data gathered outside the colored regions in Figure 3.

	N	Mean momentum flux (mPa)			% of zonal flux explained by	
		Zonal	Eastward	Westward	Geom. mean	Geom. σ
Indian Ocean	149898	0.21	1.42	1.21	48	55
Tropical Pacific	166494	0.05	1.39	1.33	71	51
Tropical Atlantic	67140	-0.82	1.37	2.19	94	-8
Extratropical Pacific	126314	0.29	1.26	0.97	86	0
Extratropical Atlantic	87087	-1.16	1.84	3.00	90	-4
Southern Ocean	1390060	-1.64	1.97	3.61	75	17

Table 1. Regional mean momentum fluxes. *N* is the number of data points collected in each region.

	Geometric mean		Geometric standard deviation	
	Eastward	Westward	Eastward	Westward
Indian Ocean	-0.06	-0.10	0.47	0.42
Tropical Pacific	-0.10	-0.11	0.48	0.47
Tropical Atlantic	-0.09	0.10	0.49	0.47
Extratropical Pacific	-0.12	-0.21	0.45	0.45
Extratropical Atlantic	0.06	0.25	0.44	0.43
Southern Ocean	0.02	0.22	0.51	0.55
S.O., 0 < u < 20 m/s	-0.13	-0.01	0.47	0.46
S.O., 20 < u < 40 m/s	0.11	0.49	0.50	0.46
S.O., 40 < u < 60 m/s	0.34	0.65	0.49	0.48

Table 2. The geometric means and geometric standard deviations of the eastward and westward momentum flux distributions, for each region. The last three rows describe data in the Southern Ocean in different bands of the smoothed zonal wind.

	99^{th} percentile flux (mPa)		% of E-W difference explained by		% of mean flux due to values higher than the 99^{th} percentile	
	Eastward	Westward	Geom. mean	Geom. σ	Eastward	Westward
Indian Ocean	7.76	6.13	33	90	7	8
Tropical Pacific	9.26	9.58	-82	-133	10	11
Tropical Atlantic	8.16	14.71	74	-15	8	11
Extratropical Pacific	7.49	5.49	72	0	9	9
Extratropical Atlantic	10.14	23.29	53	-5	11	14
Southern Ocean	14.02	29.96	60	27	12	13

Table 3. Regional 99^{th} percentile momentum fluxes.